Top Catal (2017) 60:1522–1536
DOI 10.1007/s11244-017-0836-7

ORIGINAL PAPER

Operando Spectroscopy of the Gas-Phase Aldol Condensation of Propanal over Solid Base Catalysts

Ana M. Hernández-Giménez[1] · Javier Ruiz-Martínez[1] · Begoña Puértolas[2] · Javier Pérez-Ramírez[2] · Pieter C. A. Bruijnincx[1] · Bert M. Weckhuysen[1]

Published online: 24 August 2017

Abstract The gas-phase aldol condensation of propanal, taken as model for the aldehyde components in bio-oils, has been studied with a combined *operando* set-up allowing to perform FT-IR & UV–Vis diffuse reflectance spectroscopy (DRS) with on-line mass spectrometry (MS). The selected solid base catalysts, a cesium-exchanged X zeolite (Cs-X), a calcium hydroxyapatite (Ca-HA) and two alkaline metal-grafted ultrastable Y (Na- and Rb-USY) zeolites, were characterized ex-situ by FT-IR after CO (CO-IR) and pyridine (Py-IR) adsorption and subsequent desorption. The combined *operando* spectroscopy study shows that alkaline metal-grafted USY zeolites are the most selective catalysts towards aldol dimer product formation, while the hydroxyapatite was more selective for successive aldol condensation reactions. For Na-USY and Rb-USY, the C–C coupling seems to be the rate-determining step during the surface reaction, which is the limiting stage of the overall catalytic process. In contrast, for the two more basic catalysts, i.e., Cs-X and Ca-HA desorption is limiting the overall catalytic process. Furthermore, the combined *operando* FT-IR & UV–Vis DRS methodology allowed monitoring the formation of carbonaceous deposits as a function of reaction time. In particular, for Cs-X and Ca-HA the rapid formation of carbonaceous deposits was observed consisting of (poly-)aromatics and highly conjugated structures, respectively. The physicochemical properties of Ca-HA with strong basic sites and moderate acidity limit its deactivation despite the observed coke formation. On the other hand, both USY catalysts were more efficient in suppressing coke formation likely due to the moderate strength of their active sites.

Keywords Aldol condensation · Bio-oil · *Operando* spectroscopy · Base catalysts · Coke

1 Introduction

Bio-oils obtained by pyrolysis are chemically complex and do not have yet the desired characteristics of a transportation fuel [1]. Indeed, the bio-oil generally has a very low heating value due to its high oxygen and water content and is strongly corrosive (pH 2–4) and highly viscous. It is also immiscible with conventional crude oil-derived transportation fuels due to its poor chemical stability [2]. Consequently, there is a clear need for extensive upgrading of such bio-oils.

Given the high aldehyde content of pyrolytic bio-oils (up to 20 wt%), aldol condensation is particularly attractive as key intermediate deoxygenation reaction in bio-oil upgrading [3, 4]. It allows one to reduce bio-oil corrosiveness as well as the oxygen content. Additionally, this C–C coupling reaction leads to an increase in the average carbon chain length [5]. In the aldol condensation reaction, as outlined in Scheme 1 for propanal, an enolizable aldehyde (or ketone) reacts with a second carbonyl compound to yield a β-hydroxyaldehyde addition product, which after dehydration forms an α,β-unsaturated ketone, which then can further

Electronic supplementary material The online version of this article (doi:10.1007/s11244-017-0836-7) contains supplementary material, which is available to authorized users.

✉ Bert M. Weckhuysen
b.m.weckhuysen@uu.nl

[1] Inorganic Chemistry and Catalysis, Debye Institute for Nanomaterials Science, Utrecht University, Universiteitsweg 99, 3584 CG Utrecht, The Netherlands

[2] Department of Chemistry and Applied Biosciences, Institute for Chemical and Bioengineering, ETH Zurich, Vladimir-Prelog-Weg 1, 8093 Zurich, Switzerland

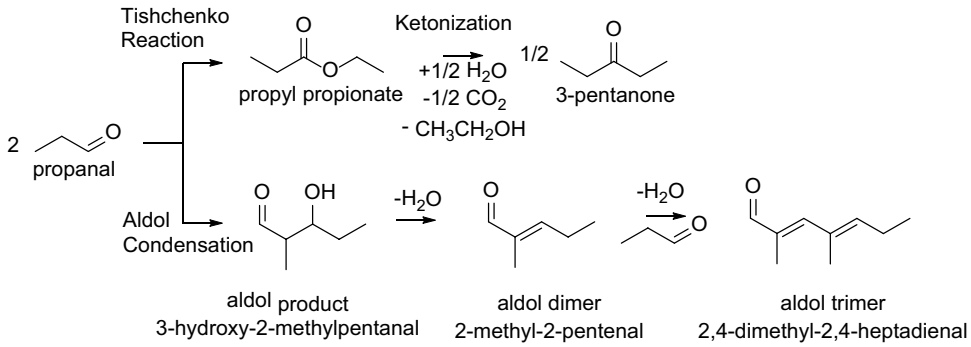

Scheme 1 Scheme of two possible routes for the self-reaction of propanal

react to, e.g., a trimeric aldol condensation product. This reaction can be acid- or base-catalyzed [6–8] using either homogeneous [9] or heterogeneous catalysts. For the latter systems, solid base materials are preferred, given the higher selectivity and better stability (*i.e.*, suffering less from coke formation) [10]. Solid bases activate the substrate by deprotonation at the α-position to give an enolate, while any (Lewis) acidic sites of weak strength present on the material can enhance the electrophilicity of the carbonyl carbon atoms [11]. Although acidic and basic sites can thus synergistically catalyze this reaction [12], ensuring a low concentration in acid sites is important in order to avoid any side reactions. Examples of such side reactions include Tishchenko ester formation, which can undergo subsequent ketonization with the evolution of CO_2 and water [13].

Solid basic oxides have been extensively used for the base-catalyzed aldol condensation of aldehydes both in the vapor [7, 14] and liquid phase [6]. Recently, Pérez-Ramírez et al. reported on the gas-phase aldol condensation reaction using alkali-exchanged X-type zeolites [15] and mesoporous hierarchical USY zeolites [16]. Most recently, USY subjected to alkali metal grafting in alcoholic media was shown to display enhanced activity and stability [17]. Other catalysts such as calcium hydroxyapatites (Ca-HA) were also shown to be active in aldol condensations [18, 19]. The hydroxyapatites, represented by the formula $Ca_{10-Z}(HPO_4)_Z(PO_4)_{6-Z}(OH)_{2-Z}{\cdot}n(H_2O)$; $0 < Z \leq 1$, contain both basic and acidic sites [20]. Notable other examples of the use of hydroxyapatites as catalyst in other gas-phase, base-catalyzed C–C coupling reactions include the Guerbet reaction of ethanol [20–22] and the Lebedev ethanol-to-butadiene process [20].

In this work, a detailed *operando* spectroscopy study on the self-condensation of propanal, used as a model for the aldehydes found in pyrolytic bio-oils, is reported over a selection of solid base catalysts. Four distinct catalyst materials were selected based on their earlier reported differences in catalytic activity; *i.e.*, Cs-X [15], Ca-HA [19] and Na-USY and Rb-USY [17]. More specifically, the two alkali metal-grafted USY zeolites were found to be the most selective towards the formation of the aldol dimer product, whereas the Ca-HA catalyst showed a high selectivity to the aldol trimer product, obtained via consecutive aldol condensation reactions. Indeed, *operando* spectroscopy studies can provide fundamental insight into the origin of the observed differences in catalytic performance and stability, as well as into related pathways of catalyst deactivation. In heterogeneous vapour phase catalysis only a few *operando* spectroscopy studies have been reported on C–C coupling reactions, however. Huber and co-workers used *operando* DRIFTS with on-line gas chromatography (GC) to investigate the condensation of butanal over alkali earth metal oxides [7], showing that besides aldol condensation other side reactions, such as Tishchenko, ketonization and cross condensations, also occur. Another *operando* DRIFTS study with on-line GC reports on the conversion of methylbutynol over ZnO [23], which had the study of different mechanistic routes as the main objective.

Here, we demonstrate a combined *operando* FT-IR and UV–Vis Diffuse Reflectance Spectroscopy (DRS) methodology with on-line Mass Spectrometry (MS) as a powerful tool to gain new insight into the aldol condensation of propanal and the possible modes of deactivation of the four selected solid bases. Time-on-stream analysis of the evolution of carbonaceous species clearly shows differences in both rate and composition of these carbonaceous deposits over the different catalytic materials. Notably, both alkaline metal-grafted USY zeolites show the highest resistance against coking, which is probably related to the moderate strength of the active sites, as further confirmed by ex-situ FT-IR analysis of the catalytic solids with CO and pyridine as probe molecules for acid-base characterization. Finally, the observed differences in amount of deposited coke were corroborated with Thermogravimetric Analysis (TGA) of the spent catalyst materials.

2 Experimental

2.1 Materials

Propanal (Acros Organics, 99%) and 2-methyl-2-pentenal (Acros Organics, 97%) were used as received. The selected

catalysts were Cs-X, a X-type zeolite exchanged with Cs^+ cations and modified under acid washing step [15]; Ca-HA, a calcium hydroxyapatite with a molar ratio Ca/P of 1.67 [19]; and alkali metal-grafted USY zeolites prepared by the treatment of high-silica USY zeolite in 0.1 M NaOH (Na-USY) and 0.05 M RbOH [17]. The properties of the catalyst materials under study are summarized in Table 1.

2.2 Catalyst Characterization

For adsorption of CO as probe molecule followed by FT-IR spectroscopy, self-supported wafers of ~10 mg and ~12 mm diameter were pressed with a pressure of 10–30 MN/m^2 for 10 s. The wafer was placed in a well-sealed FT-IR cell connected to an oven. The wafer was dried by heating the samples to 400 °C with a heating rate of 5 ºC/min for 1 h under vacuum (~10^{-3} mbar). A Perkin-Elmer System 2000 instrument was used to record the FT-IR spectra in transmission mode in the spectral range of 4000–400 cm^{-1}. For each spectrum 25 scans were collected with a spectral resolution of 4 cm^{-1}. The spectrum of the empty cell was taken as background. Spectra of each sample were taken at low temperature (*i.e.*, −188 °C) during CO (10% in He, purity 99.9%) adsorption/desorption, at low pressures (between 10^{-3} and 10 mbar). The FT-IR spectra obtained were normalized to the characteristic vibrational features of the catalyst material.

Similarly, for FT-IR after pyridine adsorption, a self-supported wafer was placed in the FT-IR cell and adsorbed water was removed by heating the sample to 400 °C with a heating rate of 5 ºC/min for 1 h under vacuum (~10^{-5} mbar). Spectral resolution and scans per spectrum were the same as in the CO adsorption experiments. Gaseous pyridine was adsorbed at room temperature (p_{Py} ~2 mbar). After 30 min of adsorption, pyridine was evacuated using a high vacuum pump system. The FT-IR spectra were continuously collected during desorption and upon increasing the temperature from 50 to 400 °C. All FT-IR spectra have been normalized to characteristic vibrational features of the catalyst material: *i.e.*, 2940–2885 cm^{-1} for Cs-X, 2250–1900 cm^{-1} for Ca-HA, and 2100–1800 cm^{-1} for alkali metal-grafted USY zeolites.

Integration of the relevant bands in the normalized FT-IR spectra was done using the BlueprintXAS software [24]. This Matlab-based software uses a holistic model, which includes the spectra of the fresh catalyst as baseline. For each spectrum 10 fits were attempted to explore the solution space of all parameters (including the peak areas, width at half maximum and peak positions) based on the methodology implemented in this program to generate the fits from unbiased starting points. As a result, a set of good fits, based on minimum sum of squared errors in the region of interest was selected for an estimation of the peak areas along with their uncertainties.

TGA-MS analyses were performed with a Perkin Elmer Pyris 1 TGA thermogravimetric analyzer coupled to a Pfeiffer Vacuum Omnistar mass spectrometer. Around 10 mg of sample was employed for TGA-MS of the fresh and spent catalysts. The spent catalysts consisted of ones exposed to a maximum of 10 min of desorption (*i.e.*, flushed with N_2 at 400 °C) after reaction. An air stream of 60 mL/min was employed during TGA-MS analysis, which consisted of heating the sample up to 900 °C with a heating rate of 5 ºC/min. The MS detector was set to monitor the evolution of H_2O and CO_2.

Table 1 Overview of the physicochemical and acid–base properties of the catalyst materials under study

Catalysts	V_{pore}[a] (cm^3/g)	S_{BET}[b] (m^2/g)	Basicity		Acidity		
			Conc.[c] (μmol/g)	Strength[c]	Nature[d,e]	Strength[d,e]	Conc.[*e] (μmol/g)
Cs-X[1] (FAU, X-type, Si/Al = 1.8, Cs/Al = 0.73)	0.39	95	500	Weak and strong	LAS	Moderate	1613
Ca-HA[2] (Hydroxyapatite $Ca_{10}(PO_4)_6(OH)_2$ calcined 600 °C	0.40	63	20	Weak and strong	LAS	Very weak	95
Na-USY[3] (Si/Al = 405 0.1 M Na^+, MeOH)	0.51	615	50	Weak	LAS	Weak	26
Rb-USY[4] (Si/Al = 400, 0.05 M Rb^+, MeOH)	0.46	531	40	Weak	LAS	Very weak	6

The pore volume, surface area and concentration of basic sites were obtained from refs. [15, 17, 19]

LAS Lewis acid sites

Determined by: [a]t-plot method, [b]BET method, [c]CO_2-TPD, [d]CO-IR (Fig. 1), [e]Py-IR, after desorption at 150 °C (Fig. 2)

Original notation of the samples used: [1]X-NH_4-AW1-Cs [15], [2]Ca-HA-1.67 [19], [3]USY-0.1 M NaOH–MeOH, [4]USY-0.05 M RbOH-MeOH [17]

2.3 *Operando* FT-IR & UV–Vis Diffuse Reflectance Spectroscopy

The experimental set-up used to monitor the reaction under *operando* conditions by combining FT-IR and Ultraviolet–Visible (UV–Vis) Diffuse Reflectance Spectroscopy (DRS) with on-line monitoring of the gas outlet by MS is shown in Fig. S1. *Operando* FT-IR spectra, once background-corrected for the KBr windows of the reaction cell, were recorded on a Bruker Tensor 27 instrument equipped with an internal room temperature DLaTGS detector. 32 scans were collected per spectrum with a spectral resolution of 4 cm^{-1} and the scanned region was 4000–400 cm^{-1}. As illustrated in Fig. S1, a UV–Vis probe was positioned at the same spot as the IR beam. *Operando* UV–Vis DRS spectra were collected of the 230–900 nm spectral region by an AvaSpec-2048L using an AvaLight DH-S-BAL probe with optical fibers for illumination and another fiber for the collection of the reflected light. Prior to the recording of the UV–Vis DRS spectra with time-on-stream, a reference measurement was recorded on a fresh sample placed inside the reaction cell, once activated. Such a background correction differs from the standard "white standard", [25] but allows for correction of both the KBr window and catalyst features, minimizing experimental error as a result of possible altering of the position of the sample inside the reaction cell. On-line MS data have been collected with an Omnistar Pfeiffer Vacuum QMS 200 mass spectrometer with quadrupole detector. The data were recorded using the program Quadstar 32-Bit.

The aldol condensation reactions with propanal were carried out in the gas-phase for 1 h at atmospheric pressure and a reaction temperature of 400 °C, which is a typical temperature for the outlet of a pyrolytic stream [1]. Each of the catalyst materials were shaped as self-supported wafers (~10 mg, 12 mm in diameter) by applying a pressure of 10–30 MN/m^2 for 10 s before being placed inside the reaction cell and measured by a combination of *operando* FT-IR and UV–Vis DRS spectroscopy with on-line MS. Prior to the reaction, the catalyst materials were firstly activated at 150 °C for 30 min and heated to 400 °C (5 °C/min) for another 30 min under a 10 mL/min of O_2 flow (99.999%, Linde). The carrier gas used during reaction was N_2 (99.999%, Linde), with a flow rate of 5 mL/min. The propanal-containing saturator was introduced into an ice bath to keep a constant temperature of 0 °C, resulting in a partial pressure of 0.13 atm. This stream is diluted by a second stream of 5 mL/min N_2, giving a final concentration of 6.1 vol% of propanal. Over the course of the reaction a total amount of 39 mL of propanal vapor was introduced into the spectroscopic reaction cell, corresponding to a WHSV of 4.2 g propanal/(h·g catalyst). After 1 h of reaction the propanal feedstock was stopped, after which the catalyst material was flushed with nitrogen (10 mL/min) at a reaction temperature of 400 °C for a fixed time to study desorption.

3 Results and Discussion

3.1 Catalyst Characterization

3.1.1 Carbon Monoxide FT-IR Spectroscopy

Complementary to the characterization data previously reported for these samples (Table 1 [15, 17, 19]), the intrinsic acid strength of the Brønsted (BAS) and Lewis acid sites (LAS) was probed by FT-IR analysis after the adsorption and desorption of CO and pyridine as probe molecules. The amphoteric nature of CO in addition provides further insight into the basicity of the samples [26]. Figure 1 shows the FT-IR spectra of the OH (Fig. 1a, c, e, g) and CO (Fig. 1b, d, f, h) stretching region collected for the four catalyst materials during CO adsorption.

For Cs-X (Fig. 1a), the weak interactions of silanol groups [27, 28] with CO, at ~3716 cm^{-1}, demonstrates its lack of BAS. This absence of Brønsted acidity is a result of the efficiency of cation exchange during the material's synthesis. Expectedly, the CO stretching region revealed the presence of strong LAS for this sample (Fig. 1b). The Cs^+ Lewis acid sites are characterized by spectral features in the region 2264–2240 cm^{-1}. Also, the band at 2121 cm^{-1} might be caused by the coordination of CO to the electrophilic Cs^+ centers via its C atom (O=C…Cs^+) [29]. At high CO pressure, absorption bands at 2141 and 2132 cm^{-1} can be observed, attributed to physisorbed CO, while the shoulder at 2149 cm^{-1} is associated to CO on coordinatively unsaturated Al^{3+} Lewis acid sites [30].

For Ca-HA (Fig. 1c) the OH stretching area is virtually unperturbed by the CO adsorbed, in line with the non-acidic character of the OH groups present [19]. The sharp band at 3573 cm^{-1} is due to contributions from surface and bulk OH groups [31, 32]. Some minor perturbations are observed in the 3600–3700 cm^{-1} spectral range and these features can be attributed to P-OH groups acting as weak basic sites. Other evidence for basicity are bands formed at 1447 and 1409 cm^{-1} (inset Fig. 1c), which correspond to carbonate species formed by strongly basic OH groups [32]. Carbonation, initially present in the beginning of the test, could be due to contamination of the hydroxyapatite with CO_3^{2-} ions coming from atmospheric CO_2 when synthesized in air or storage [32]. Meanwhile the more intense bands at 1579 and 1547 cm^{-1} are related to surface $(PO_x)_s$-carbonates formed by weak PO_3^{4-} sites of the hydroxyapatite material [31]. In addition, the bands detected at 2179 and 2169 cm^{-1} in the CO stretching region (Fig. 1d) indicate the presence of some weak LAS [33].

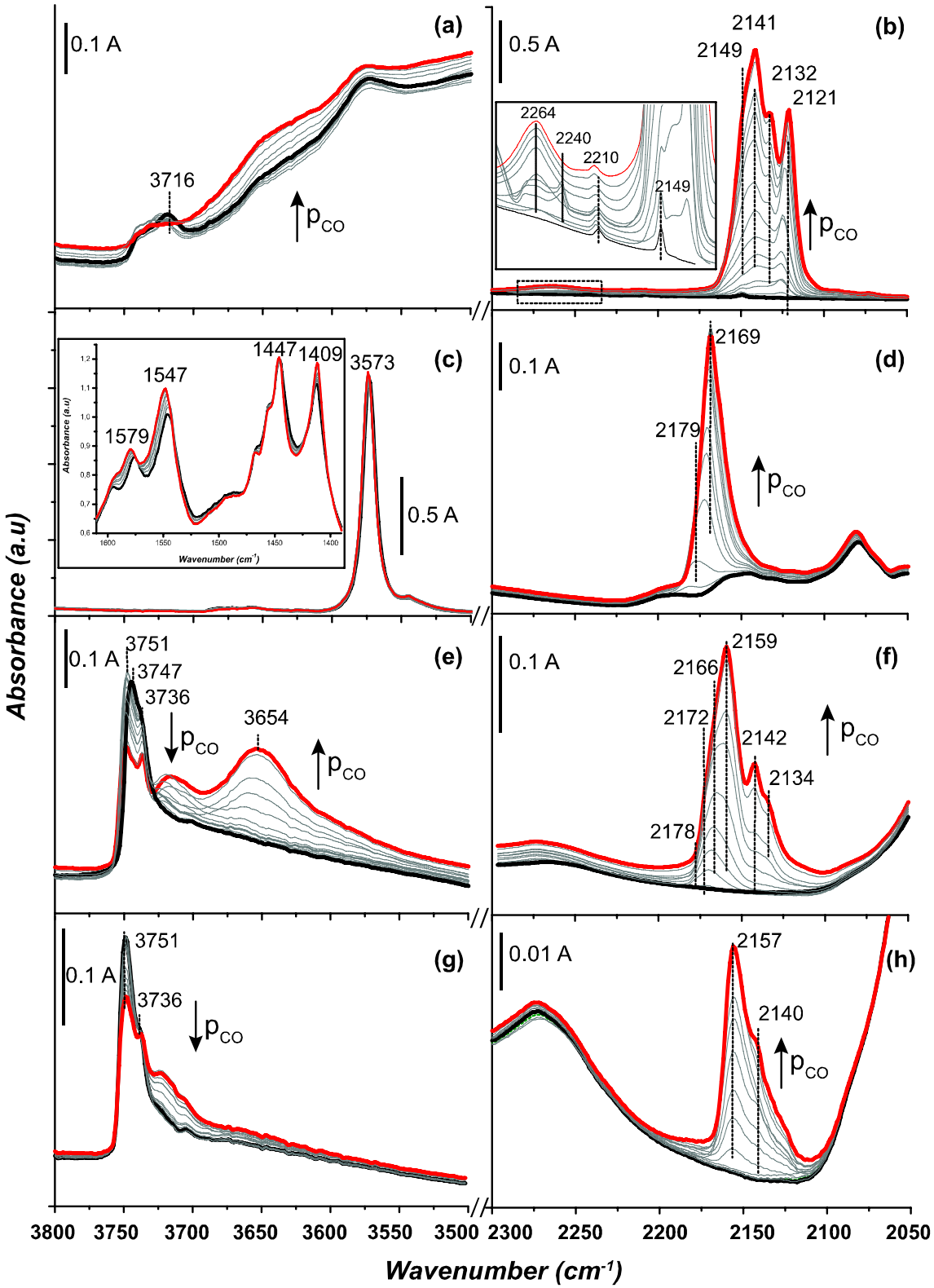

Fig. 1 FT-IR spectra of the catalyst materials during CO adsorption at 85 K in the OH stretching region (**a, c, e, g**) and in the CO stretching region (**b, d, f, h**): **a, b** Cs-X, **c, d** Ca-HA, **e, f** Na-USY, **g, h** and Rb-USY. The initial spectrum is marked in *black*; the *red* spectrum was taken at the maximum CO coverage

For Na-USY (Fig. 1e), the free silanol groups observed at 3747 cm^{-1} before CO exposure, partially disappear upon CO adsorption and shift to 3654 cm^{-1}. These hydroxyl species are known to be located in the supercages of zeolite Y and can be considered as isolated and very weak BAS, as the small shift $\Delta\nu = 94$ cm^{-1} indicates [34, 35]. The $\Delta\nu$ shift is proportional to the acid strength of the OH group [34]. The band at 2172 cm^{-1} (Fig. 1f) can be attributed to CO adsorbed on Na^+ Lewis acid sites [28]. More intense bands at 2166 and 2159 cm^{-1} are associated with CO adsorbed on silanol groups, meanwhile the weak band at 2179 cm^{-1} is thought to derive from the extinguished BAS of the parent USY zeolite. Physisorbed CO was also observed at 2142 and 2134 cm^{-1} [35].

For the Rb-USY sample (Fig. 1g) the free external silanol groups, centered at 3751 cm^{-1}, show almost no acidic character [34–37]. Only weak bands, at high coverages of CO ($p_{CO} > 3$ mbar), appear in the CO spectral region (Fig. 1h). The band at 2157 cm^{-1} appears as a consequence of weak CO interactions with external silanol groups, with the band at 2140 cm^{-1} corresponding to physisorbed CO. Note that for neither of the two USY samples under study an absorption band at ~2260 cm^{-1} was detected, which is known to be associated with strong LAS. Consequently, in these samples (and in contrast to the Cs-X sample) the cations must be located in more inaccessible positions, e.g. the sodalite cages [38].

3.1.2 *Pyridine FT-IR Spectroscopy*

Figure 2 shows the FT-IR spectra collected for the four catalyst materials during pyridine adsorption at room temperature and subsequent desorption.

The FT-IR spectra after pyridine adsorption and subsequent desorption further corroborate the findings obtained with CO as probe molecule. Indeed, the lack of a band at ~1545 cm^{-1} [39, 40] confirms that there are practically no strong BAS on any of the catalyst materials. Along these lines, the weak perturbations at ~1555 and 1595 cm^{-1}, associated to the ring vibration 8a mode of pyridine (according to the nomenclature introduced by Kline et al. [41]) are seen for the alkaline metal-grafted USY zeolites and could be due to hydrogen-bonded pyridine with weakly acidic silanol groups [27, 42]. On the contrary, LAS can be observed in every catalyst material. In the case of Cs-X (Fig. 2a) bands at 1597 and 1440 cm^{-1} are thought to correspond to pyridine adsorbed on Lewis acidic Cs^+ cations [27]. By progressive outgassing the materials, these absorption bands decrease in intensity and were no longer detected after outgassing at 150 °C, in the case of Na- and Rb-USY catalysts, and 300 °C (not displayed) in the case of Cs-X and Ca-HA, suggesting that these acid sites are not strong [39]. For Ca-HA (Fig. 2b) bands emerged at 1600, 1573, 1488 and 1445 cm^{-1} [33], and decrease with increasing outgassing temperature indicating the weakness of the LAS. Very weak LAS are detected for the Na-USY zeolite material (Fig. 2c) as characterized by the band at 1443 cm^{-1} [28, 39] which desorbs

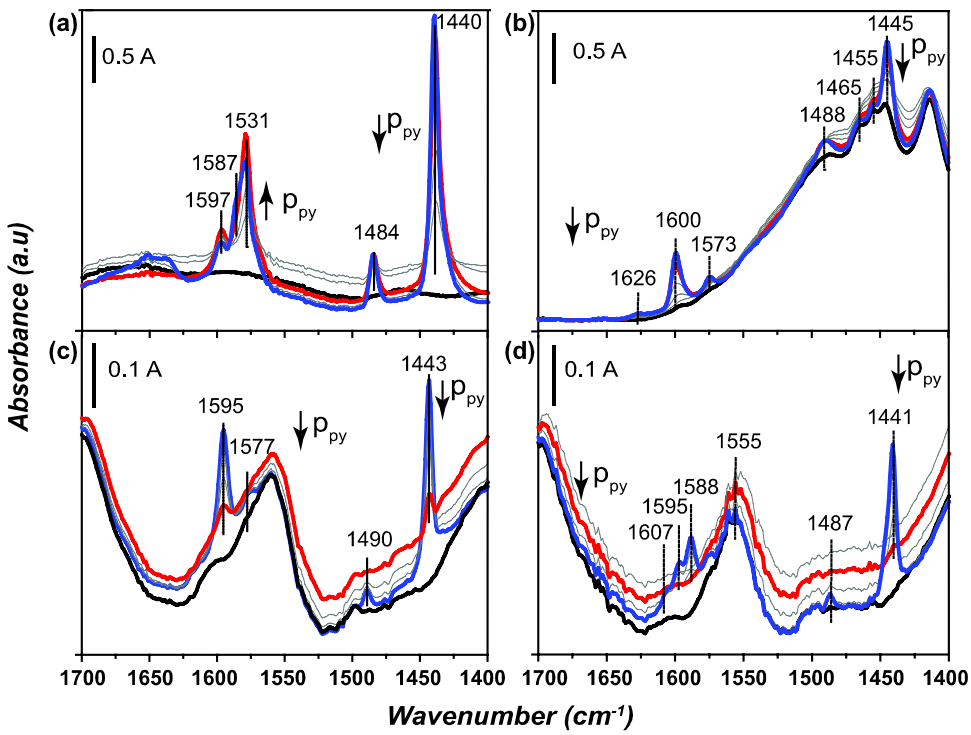

Fig. 2 FT-IR spectra of the catalyst materials during pyridine desorption from room temperature (*blue*) to 150 °C (*red*): **a** Cs-X, **b** Ca-HA, **c** Na-USY and d Rb-USY. The spectrum before pyridine exposure is marked in *black*

at low temperature (<150 °C). Even weaker are the LAS in the Rb-USY zeolite material (Fig. 2d), as evidenced by the absorption band at 1441 cm^{-1}, which practically disappeared upon increasing outgassing temperature.

The amount of LAS for each catalyst material under study was calculated based on Eq. 1, derived from Beer´s law applied to dδ (cm^{-1}) [39]. In Eq. 1 A (cm^{-1}) represents the integral under the curve delimited by dδ (cm^{-1}) (band at 1440–1445 cm^{-1}), ε is the extinction coefficient at 150 °C, previously determined as 2.22 cm/μmol and reported by Emeis [39], and ρ is the mass (mg) of the wafer per cm^2 through which the beam is sent (effective cross-section). Py:LAS stoichiometry was assumed to be 1:1, *i.e.*, only one Py molecule is adsorbed per accessible Lewis acid site. The results of this quantification procedure are included in Table 1, providing clear differences in the amount of acid sites; *i.e.*, Cs-X >>> Ca-HA > Na-USY > Rb-USY.

$$[LAS] = \frac{A \cdot 10^3}{\varepsilon \cdot \rho} \quad (1)$$

3.2 *Operando* FT-IR & UV–Vis Diffuse Reflectance Spectroscopy

3.2.1 Operando FT-IR Spectroscopy

The time-resolved *operando* FT-IR spectra obtained for the four catalyst materials, described in Table 1, are shown in Fig. 3. The peak assignments are listed in Table 2.

The time-resolved FT-IR spectra obtained for the Cs-X zeolite (Fig. 3a) shows negative intensities at 3732 and 3572 cm^{-1} suggesting interactions of reagent/products with the few silanol groups of the sample (Fig. 1a). Within the first minutes of reaction, bands in the range 2963–2718 cm^{-1} emerge and are ascribed to aliphatic C–H stretching (ν_{C-H}) vibrations. Although the assignment of these bands is not straightforward, the band at 2718 cm^{-1} can be unambiguously assigned to a Fermi resonance structure of the CH stretching vibrations from aldehydes [43, 45, 46]. After two minutes of reaction, a ν_{C-H} band arises at 3047 cm^{-1}, most likely originating from aromatic species [43]. This band correlates with the increase in absorption of a strong band centered at ~1590 cm^{-1} attributed to C=C stretching ($\nu_{C=C}$) of carbonaceous species (coke) [48–52]. In the carbonyl stretching ($\nu_{C=O}$) region, the propanal absorption at 1759 cm^{-1} is almost unnoticed compared to the other $\nu_{C=O}$ band at 1700 cm^{-1}, assigned to an α,β-unsaturated compound, *i.e.*, the aldol dimer product, 2-methyl-2-pentenal, as the experimental bands derived from its adsorption onto the catalyst indicate (Fig. S3a [44, 47]). The $\nu_{C=C}$ band of the enol group of the aldol dimer quickly develops at 1687 cm^{-1} (Fig. S3a). Another $\nu_{C=O}$ band arises at 1714 cm^{-1}, which is assigned to the side product 3-pentanone (Scheme 1). Other absorption bands appearing in the fingerprint region (ν < 1500 cm^{-1}) correspond to C–H bending vibrations (σ_{C-H}) of ethyl (1467 cm^{-1}) and methyl (1384 cm^{-1}) groups. After 40 min of desorption, the spectrum profile still shows FT-IR features at 3047, 1590 and 1366 cm^{-1}, providing evidence for the presence of remaining carbonaceous deposits.

The time-resolved IR spectra for Ca-HA (Fig. 3b) show surface P-OH and lattice OH^- groups (3670 and 3566 cm^{-1}) involved in the adsorption of species and/or catalysis, in a similar way to the interactions of CO with OH stretching bands indicated in the Cs-X zeolite. After 2 min of reaction, bands in the C–H stretching region ascribed to aliphatic aldehyde (*i.e.* propanal) (2972–2720 cm^{-1}) and to aromatic/olefinic species (3058 cm^{-1}) are observed. In the carbonyl stretching region and immediately after starting reaction, the $\nu_{C=O}$ of propanal emerges with a doublet at 1760 and 1734 cm^{-1}, indicative of both gas phase and chemisorbed propanal, respectively [45]. With increasing time-on-stream both absorption bands increase till saturation levels (Fig. S7), with the 1734 cm^{-1} band associated to adsorbed propanal increasing more than the 1760 cm^{-1} band. The $\nu_{C=O}$ and $\nu_{C=C}$ bands, ascribed to the aldol dimer, arise within the first 2 min of reaction at 1705 and 1670 cm^{-1} accompanied by its σ_{C-H} bands at 1404 and 1379 cm^{-1}. Bands at 1544 and 1441 cm^{-1} are identified as carbonate species, initially present. The carbonation of the catalyst is a consequence of the adsorption of species on strong basic sites, leading to a rearrangement between Ca^{2+} cations of the Ca-HA and lattice OH^- groups [31]. Nevertheless, poisoning of the basic sites by CO_2 only affects the active sites working at the beginning of the reaction, those still working at steady state being not impacted. With increasing time-on-stream another $\nu_{C=C}$ band arises at 1640 cm^{-1}, likely due to the formation of the aldol trimer [46, 47]. As for the Cs-X catalyst material, most absorption bands disappear upon desorption, except for the $\nu_{C=C}$ band associated with carbonaceous deposits. The ν_{C-H} band assigned to carbonaceous species (3058 cm^{-1}) is significantly weaker than for Cs-X, though. It could mean either that coke forms more extensively on the Ca-HA catalyst relative to the Cs-X material.

The FT-IR spectra for Na-USY are represented in Fig. 3c. The negative intensity seen for the unconstrained hydroxyls [53] at 3732 cm^{-1} indicates its involvement in the adsorption and/or catalysis. Within the first moments of the catalytic reaction, propanal spectral features emerge at 2976, 2940, 2812 and 2720 cm^{-1}, for the ν_{C-H} vibrations, as well as 1763 and 1735 cm^{-1} for the $\nu_{C=O}$ vibrations. After 5 min of reaction the $\nu_{C=O}$ stretching bands of the aldol dimer weakly appear at 1706 cm^{-1}, accompanied by the conjugated $\nu_{C=C}$ vibration at 1690 cm^{-1} (Fig. S5a). The absorption band emerging at 1717 cm^{-1} is again associated with the formation of 3-pentanone. Coke formation is noted by the appearance of a weak stretching band at 3063 cm^{-1} and the

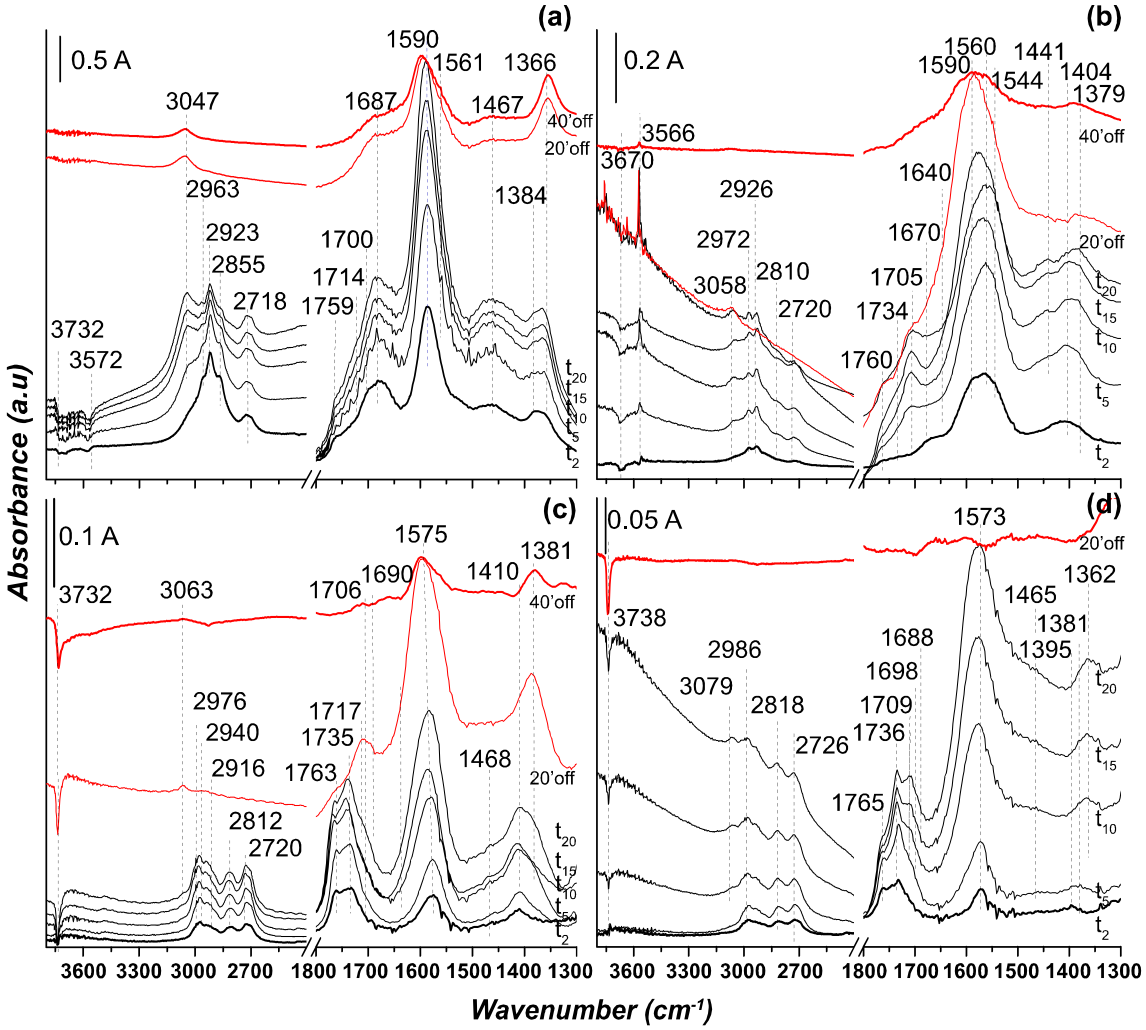

Fig. 3 Background-corrected FT-IR spectra over the first 20 min of gas-phase conversion of propanal at 400 °C over: **a** Cs-X; **b** Ca-HA; **c** Na-USY; **d** Rb-USY. *Highlighted in red* are the selected spectra during the desorption process, recorded 20 and 40 min after switching off the propanal feed after 1 h of reaction, at 400 °C

stronger $\nu_{C=C}$ signal at 1575 cm^{-1}. These spectral features are retained after 40 min of desorption, and consequently the absorption band associated with external silanol groups does not fully recover, indicating that carbonaceous species remain anchored.

Within the first moments of the catalytic reaction, the FT-IR features of the Rb-USY sample (Fig. 3d) are very similar to those of the Na-USY sample (Fig. 3c). Nevertheless, the early appearance of the absorption bands at 1709 and 1698 cm^{-1} of the $\nu_{C=O}$ and $\nu_{C=C}$ vibrations of the aldol dimer, suggest a higher activity in the aldol condensation reaction, which is in line with previously reported catalytic activity tests [17]. In addition to the absorption bands corresponding to the formation of the aldol dimer, a weaker absorption band at 1688 cm^{-1} could be ascribed to the $\nu_{C=C}$ vibration of the aldol trimer. The ν_{C-H} and $\nu_{C=C}$ bands emerging at 3078 and 1573 cm^{-1} reveal that this catalyst material is also prone to the formation of aromatics and coke. After catalytic reaction, the Rb-USY catalyst material recovers faster than any other catalyst material under study. After 20 min of desorption signs of any remaining organics are less evident than for the three other discussed catalyst materials. However, compared to Na-USY, more aromatics are observed for the Rb-USY (as measured by the ratio $\nu_{C=C}$ coke/$\nu_{C=O}$ product). Nevertheless, the Rb-USY catalyst material presents better recoverability, which might be related to the more moderate acid character of the free silanol groups.

It is important to note that the FT-IR spectra look very different for the alkaline metal-grafted USY zeolites compared to Cs-X and Ca-HA. For both Na- and Rb-USY catalysts (Fig. 3c, d) the FT-IR features of the reagent dominate over those of the product, underlining that the surface reaction is limiting [54] in this case. Previously, it has been

Table 2 Assignment of the main FT-IR peaks for the reference compounds of interest adsorbed over the catalyst materials used in this work

Position (cm^{-1})	Assignment	Mode	Species	References
~3050–3080	ν(C–H)	Stretching	Aromatics/olefins	[43]
2963–2986	ν(C–H)	ν_{as} (–CH_3) (asymmetric)	Propanal/aldol dimer	[43–45], Fig. S2–S6 (a)
2923–26	ν(C–H)	ν_{as} (–CH_2–)	Propanal	[43–45], Fig. S2–S6 (a)
2940	ν(C–H)	ν_{as} (–CH_2–)	Aldol dimer/propanal	[43–45], Fig. S2–S6 (a)
2915	ν(C–H)	ν_{s} (–CH_2–)	Propanal	[43–45]
2905	ν(C–H)	ν_{s} (–CH_3)	Propanal	[43–45]
2810–2855; 2718–2726	ν(C–H)	ν(CO–H); doublet (Fermi resonance)	Propanal/dimer	[43–45], Fig. S2–S6 (a)
1759–1763; 1735	ν(C=O)	Stretching, overtone (doublet)	Propanal	[45]
1709–1717	ν(C=O)	Stretching	3-Pentanone	[43, 44]
1687–1706	ν(C=O)	Stretching	Aldol dimer/trimer	[43, 44, 46, 47] Fig. S2–S6 (a)
1670–1690	ν(C=C)	Stretching, shoulder	Aldol dimer	[43, 44, 46, 47] Fig. S2–S6 (a)
1640	ν(C=C)/σ(O–H)	Stretching, shoulder/Bending	Aldol trimer/water	[46, 47], Fig. S3 (a)
1573–1590	ν(C=C)	Stretching	"Coke"	[48–52]
1465	σ(C–H)	Scissors, CH_2–CH_3	Propanal/aldol dimer	[43–47]
1395/1410	σ(C–H)	Bending (–CH_2–CO)	Propanal/aldol dimer	[43–47]
1362/1381	σ(C–H)	Bending (CH_3–) sym	Propanal/aldol dimer	[43–47]

suggested that propanal condensation follows a single-site Eley–Rideal mechanism and the observed reaction order of 1 for propanal was suggested to be due to either a surface reaction or the desorption step being rate-limiting [55]. In this case, the spectra suggest it would be the latter. For the different steps involved in the surface reaction, i.e. enolization of propanal, C–C coupling and dehydration, C–C coupling would be then be rate-determining. For Cs-X and Ca-HA (Fig. 3a, b) the spectra suggest the desorption step to be the reaction rate-limiting, given the fact that FT-IR features of product adsorbed onto catalyst surface dominate over those of the reagent. Focusing on the surface reaction, it is meaningful that for every catalyst material under study, except for the Cs-X material, the $\nu_{as}(CH_3–)$ and σ_{CH3} bands dominate over the $\nu_{as}(–CH_2–)$ and σ_{CH2} bands. For Cs-X instead, the higher intensity of the bands $\nu_{as}(–CH_2–)$ at 2923 cm^{-1} and σ_{CH2} at 1465 cm^{-1} indicates a higher presence of more linear products, *i.e.*, 3-pentanone over the aimed aldol dimer product.

3.2.2 Operando UV–Vis Diffuse Reflectance Spectroscopy

During the catalytic reaction, the initially white catalyst wafers darkened as a result of the formation of conjugated (aromatic) species, ones that might be involved in deactivation that is observed for the different catalyst materials. The *operando* UV–Vis Diffuse Reflectance Spectroscopy (DRS) data on this process are shown in Fig. 4, while the absorption band assignments are summarized in Table 3.

For all catalyst samples under study an absorption band centered at ~260–270 nm emerged soon after exposing the solids to propanal, associated with the weak n → π* electronic transition of the carbonyl group in the aliphatic aldehyde substrate (Table 3). Correlating with the changes seen in the time-resolved FT-IR analyses, after 1 min of reaction, for Cs-X (Fig. 4a) and Ca-HA (Fig. 4b), and 2 min in the case of alkaline metal-grafted USY zeolites Fig. 4c, d, two more absorption bands emerge at ~240 and ~300 nm respectively, which are associated with π → π* and n → π* transitions of the C=C and C=O groups of the aldol dimer [45, 55] (Fig. S3b). The shift from the theoretical position of the C=C band of the dimer (at *ca*. 220 nm [46]) to the experimental one (*ca*. 240 nm) might be due to the detection limit of the equipment, which is in the range of $230 < \lambda < 1000$ nm. After 2 min the absorption band at ~300 nm, ascribed to the dimer, quickly increases in intensity at the expense of the propanal absorption band centered at ~270 nm. This absorption band then progressively redshifts with increasing time-on-stream, which might be due to an increase in the alkyl substituents, in line with the C–C coupling reaction and subsequent formation of the aldol trimer. According to estimations based on the Woodward-Fieser rules for predicting λ_{max} positions for π → π* transitions of α,β-unsaturated aldehydes [46], the position of the C=O absorption for the aldol trimer should be placed at ~376 nm. For the Cs-X (Fig. 4a) and Ca-HA (Fig. 4b) catalyst materials, after 2 min of reaction the UV–Vis spectra broaden and absorb light in the entire wavelength range. This broad absorption feature developed later for the Na-USY zeolite (Fig. 4c) and its Rb-counterpart

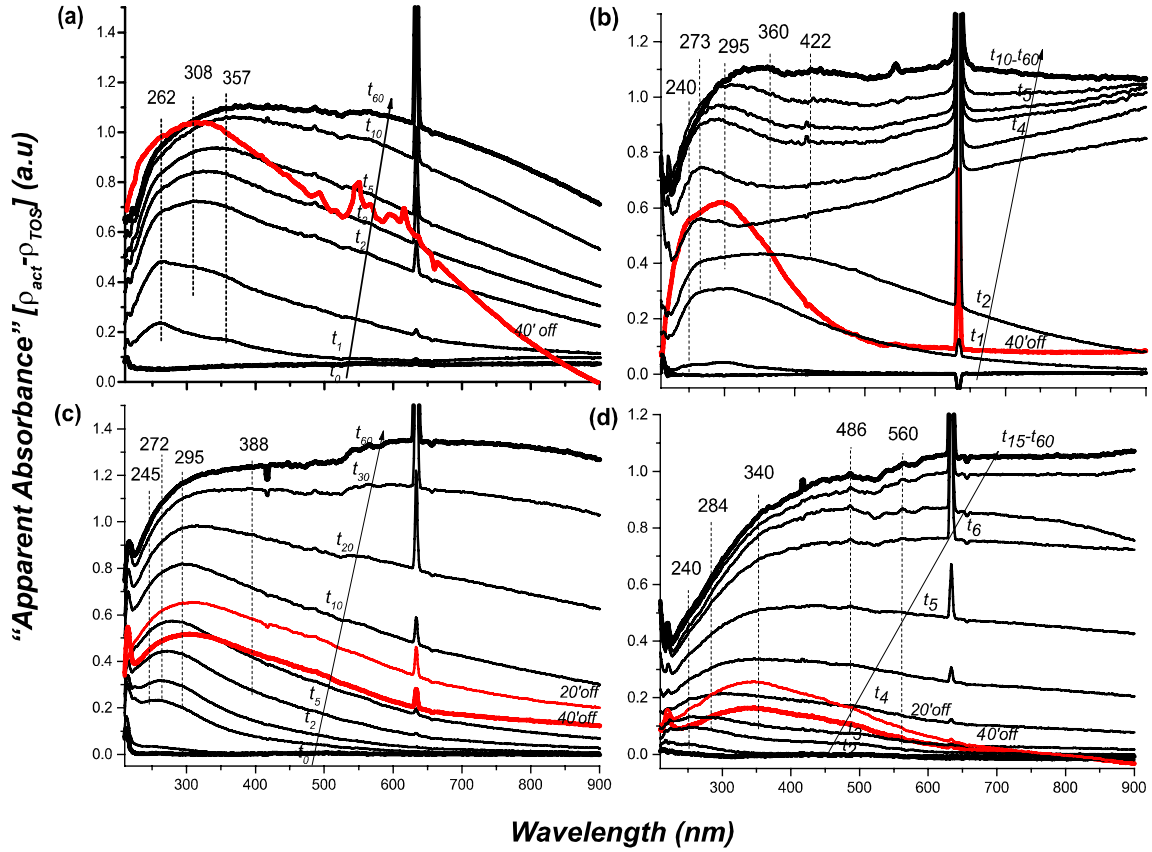

Fig. 4 Background-corrected *operando* UV–Vis diffuse reflectance spectra during the gas-phase conversion of propanal at 400 °C over: **a** Cs-X; **b** Ca-HA; **c** Na-USY; **d** Rb-USY. "Apparent absorbance" refers to the difference of reflectance of the surface species at a certain time-on-strean (ρ_{TOS}) and the reflectance of the activated catalyst (ρ_{act}) [25]. *Highlighted in red* are selected spectra recorded during desorption, after 1 h reaction, at 400 °C. The references were taken of fresh catalyst materials. Artifacts at ~420 and 650 nm are caused by the violet light of the UV–Vis probe and the red NIR beam light, respectively

Table 3 Assignments of the characteristic UV–Vis absorption bands observed during the gas-phase self-condensation of propanal conducted at 400 ºC

Range, λ (nm)	Electronic transition	Association	Absorptivity, ε	Assignment	References
230–250	π → π*	C=C	Strong	Dimer/trimer/aromatics	[46, 56] Figs. S2–S6 (b)
260–290	n → π*	C=O	Weak	Propanal	
300–330	n → π*	C=O	Weak	Dimer	
350–380	n → π*	C=O	Weak	Trimer	
>400, overall	π → π*	C=C	Strong	Coke, poly-aromatics	

(Fig. 4d). These electronic transitions are ascribed to the fast development of aromatic ring structures and carbonaceous species that could cause catalyst deactivation [52]. For the Cs-X catalyst material though, the absorption bands in the visible region tail less towards longer wavelengths compared to the other three catalyst materials. This observation could be related to a softer/less condensed composition of the coke developed over the Cs-X material, which correlates well with the rich-in-hydrogen carbonaceous deposits observed for Cs-X as measured by FT-IR (Fig. 3a). The noted signal saturation, which relates to the rate of coking, is more pronounced for Cs-X and Ca-HA (after 10 min of reaction) than for the two other samples; *i.e.*, 15 min for Rb-USY and 40 min for Na-USY.

After extensive desorption by N_2 flushing the intensities of the absorption bands at longer wavelengths considerably decrease, which indicates a certain release of volatile aromatic species. After 40 min of outgassing, a large fraction of the large aromatics (*i.e.* species absorbing at the highest wavelengths, $\lambda > 500$ nm) were released from all

catalyst materials. Additional carbonyl containing species and mono-olefinic species, which absorb light at ~300 and <250 nm respectively, still linger. In line with the FT-IR results (Fig. 3d), the decrease in absorption upon desorption is slower and less complete for Na-USY as compared to Rb-USY (Fig. 4d).

3.2.3 On-Line Mass Spectrometry

The differences seen in the *operando* FT-IR and UV–Vis DRS profiles of the various catalyst materials under study are also reflected in their catalytic performances, as monitored by on-line mass spectrometry (MS). The catalytic performance data of the different catalysts under study are summarized in Fig. 5. Ion currents were recorded for the m/z values of the propanal reactant, the aldol reaction intermediates, as well as the products water and the aldol condensation dimer and trimer products and the by-products 3-pentanone and propyl propionate. The MS fragments of the species considered are summarized in Table S1 (see also Schemes S1–S3). Selection of these m/z values was based on the database [44], if available. For species not present in the database (*e.g.*, the aldol intermediate product and the aldol trimer) fragmentation patterns were predicted, based on a methodology described elsewhere [46] to determine the most reliable ion current (Scheme S1–S3). Original ion current values obtained for each species were normalized by the corresponding initial fragmentation of each species directly bypassed to the mass spectrometer, by the value of the signal of the carrier gas (N_2, m/z = 28) and by the catalyst weight.

Figure 5 shows that shortly after commencing the reaction propanal conversion reaches a quasi-steady state with increasing time-on-stream. As expected, the aldol dimer (m/z = 41) is observed to be the dominant product for all the samples. Beyond the high selectivity towards the aldol dimer, the presence of side products, such as 3-pentanone (m/z = 86) and its precursor propyl propionate (m/z = 75), is higher for Cs-X than for the other three catalysts (Fig. 5a),

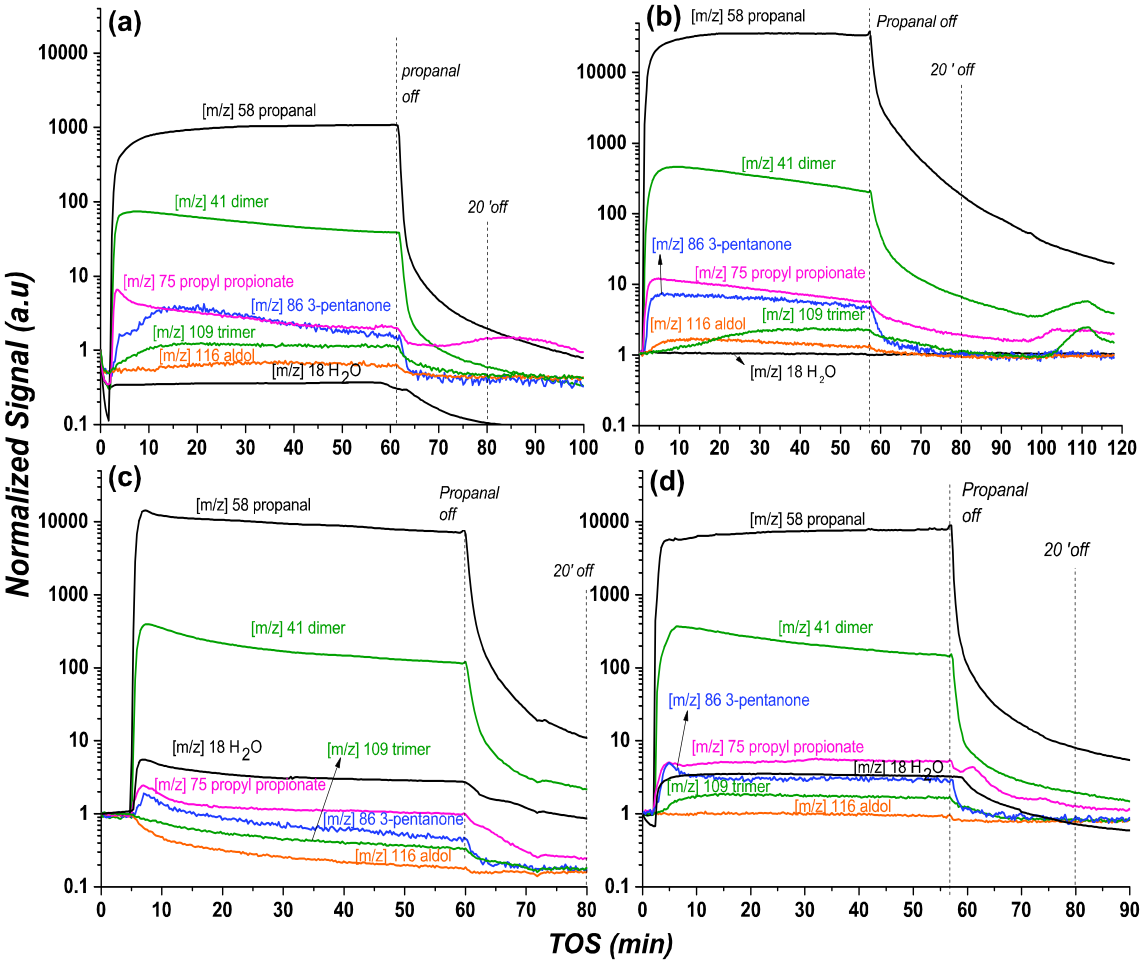

Fig. 5 On-line mass spectrometry data during the 1 h gas-phase conversion of propanal at 400 °C over: **a** Cs-X; **b** Ca-HA; **c** Na-USY; and **d** Rb-USY. The original ion current values obtained for each species were normalized by the corresponding initial fragmentation of each species directly bypassed to the mass spectrometer, by the value of the signal of the carrier gas (N_2, m/z = 28) and by the catalyst weight

as previously indicated during the catalytic tests [16] and confirming the validity of the combined *operando* spectroscopy setup used. The aldol trimer is seen most with Ca-HA, increasing at the expense of the dimer (Fig. 5b), with its high activity for consecutive aldol condensation again being in line with reported catalytic tests run in a standard microreactor [19].

The high sensitivity of the MS instrument, also allowed for the detection of various other species, including the possible aldol intermediate, 3-hydroxy-2-methylpentanal (m/z = 116); the latter compound was hardly detected for the alkaline-grafted USY zeolites (Fig. 5c, d), but was seen for the Cs-X and Ca-HA materials (Fig. 5a, b). The detection of the aldol intermediate for Cs-X and Ca-HA lead us to think that dehydration is the rate-determining step of the surface reaction, which is further supported by the low intensity of water signal during the whole catalytic reaction. In contrast for Na- and Rb-USY, for which—besides the absence of 3-hydroxy-2-methylpentanal signal—the water signal is released at substantially larger scale during reaction, the C–C coupling is considered as the rate-limiting step of the surface reaction.

Alcohol dehydrations, *i.e.* 3-hydroxy-2-methylpentanal converting into the aldol dimer product in the case at hand, are more favorable performed over acidic than over basic catalyst materials because of the preference for abstracting the H^+ of the C attached to the OH substituent (over the H^+ abstraction at C-1) [13]. Therefore, the dehydration step over the more basic catalyst materials, *i.e.*, Cs-X and Ca-HA, might become more suppressed than over the two alkaline metal-grafted USY zeolites.

3.3 Coke Amount and Composition of Spent Catalyst Materials

After reaction, the spent catalyst materials were analyzed by TGA-MS under air over a temperature range of 50–900 °C to burn off all the remaining carbonaceous species. The TGA-MS measurements were performed on samples exposed to a maximum of 10 min of N_2 flushing after reaction. The *operando* UV–Vis DRS spectroscopy results (Fig. 4) showed that after 10 min of desorption a substantial amount of species remain adsorbed on the catalyst. Weight loss as well as the evolution of H_2O and CO_2, released upon combustion of the organics, were monitored as a function of reaction temperature and time. The results are summarized in Table 4.

The TGA results show that more coke is formed on the Cs-X and Ca-HA samples than on the Na-USY and Rb-USY zeolites. Based on the observed combustion temperature the weight loss has been presented as soft and hard coke as well as graphitic-like coke [50], according to the classification proposed by Pradhan et al. [57]. The analysis of the coke composition indicates that the coke deposits on the Ca-HA sample correspond to a great extent to hard coke burning between 330 and 700 °C [49]. The other catalyst samples show a more even distribution between hard and soft coke. Hard coke is related to strongly hydrogen-deficient polyaromatic deposits [58]. In this experiment, the temperature of maximum combustion of hard coke was similar for every catalyst material, at ~400 °C (Fig. S8). The higher hydrogen content of the carbonaceous species (soft coke) for the Cs-X material is consistent with the *operando* UV–Vis DRS and FT-IR results. The UV–Vis DRS data (Fig. 4) already showed that absorption bands of coke (and related aromatics) absorb light in a wider range of wavelengths in the case of the Ca-HA, and the alkaline metal-grafted USY zeolites, consistent with increased sp^2 character, as compared to Cs-X. Indeed, for this catalyst sample much stronger C–H stretching vibrations of aromatics are observed by *operando* FT-IR spectroscopy, which is in line with a higher H/C ratio of the composition of the (poly-)aromatic species. More details about the type of coke species formed can be obtained from the FT-IR spectroscopy data. The spectra of the region of interest, as shown in Fig. 6, are of the catalyst samples after 20 min of reaction, as well as after 20 min of desorption, for comparison.

In the case of Cs-X (Fig. 6a) the coke band at ~1590 cm^{-1} [58], is sharper and better defined than for Ca-HA and Na- and Rb-USY catalysts (Fig. 6b–d). For the latter, other contributing $\nu_{C=C}$ vibrations at 1560 cm^{-1}, assigned to the C=C stretching in aromatic and highly conjugated structures (*e.g.* alkylnaphthalenes and

Table 4 Spent catalyst mass loss (%) as recorded by thermogravimetric analysis (TGA) determined after 1 h reaction at 400 °C for every catalyst material under study

Catalyst	Water Weight loss (wt%) (50–180 °C)	Coke content (wt%)			
		Soft coke (180–330 °C)	Hard coke (330–700 °C)	Graphite-like (700–900 °C)	Total coke
Cs-X	4.0	2.0	4.5	0	6.5
Ca-HA	0.5	0.6	5.4	0.4	6.4
Na-USY	0.2	1.0	2.3	0	3.3
Rb-USY	0.1	0.7	1.9	0.3	3.0

The corresponding TGA plots are shown in Fig. S8

polyethylenes) [48], shift the coke band to lower energies (~1570 cm^{-1}). The location of the band at lower energies is thus an indication of more condensed coke formed at higher reaction temperatures (*i.e.*, hard coke) [58]. In contrast, the higher energy of the coke band for Cs-X is in line with its proposed softer nature, as suggested by the TGA-MS (Table 4) and UV–Vis DRS results. After reaction, when reagent and reaction products are desorbed, the identification of the absorption bands corresponding to coke are less ambiguous. The $\nu_{C=C}$ vibration assigned to coke blueshifts thus to ~1600 cm^{-1} for Cs-X and Na- and Rb-USY zeolites, and to 1590 cm^{-1} in the case of the Ca-HA material, according to its higher amount of hard coke.

The absorption bands located in the region 1490–1510 cm^{-1} are normally assigned to bending vibrations of carbocations [58] whose weak contributions for every catalyst may suggest then little presence of linear or branched saturated hydrocarbons, as expected for polyaromatic carbonaceous species. The limited intensity after desorption of the C–H stretching modes between 2800 and 2900 cm^{-1} also suggests that little short carbocation species (and vast domain of hard coke instead) are present. In any case, the ratio of the bands ν_{C-H} $(CH_2)/\nu_{C-H}$ (CH_3) (~2930/2970 cm^{-1}) increased in the order: Ca-HA < Rb-USY < Na-USY < Cs-X, aligning with an increase in linearity and therefore a lower branching degree of aliphatic coke [58].

4 Conclusions

The activity, selectivity and stability of the solid base catalyst materials under study, namely Cs-X, Ca-HA, Na-USY and Rb-USY, were tested for the gas-phase aldol condensation of propanal using a combination of *operando* FT-IR & UV–Vis diffuse reflectance spectroscopy (DRS) measurements with on-line mass spectrometry (MS). The catalytic behavior of the materials was monitored under reaction condition, and the products detected and results obtained are in line with the kinetic tests carried out in a standard micro-reactor, demonstrating the *operando* nature of the experimental approach. This way, additional information on surface speciation and the rate determining steps of the process was obtained. With FT-IR spectroscopy and related on-line MS measurements it has been confirmed that the alkali metal-grafted USY zeolites are the most active towards the aldol dimer formation whereas, in terms of overall activity towards consecutive aldol condensation reactions, Ca-HA presents the highest selectivity towards the aldol trimer. For the Cs-X zeolite, instead, the formation of by-products, as propyl propionate and 3-pentanone, were noted to a higher extent.

Based on the *operando* FT-IR spectra, product desorption was identified as rate determining in the overall reaction over both Cs-X and Ca-HA catalysts, with the absence of propanal features revealing fast conversion. Product features are detected instead and their slow desorption limits

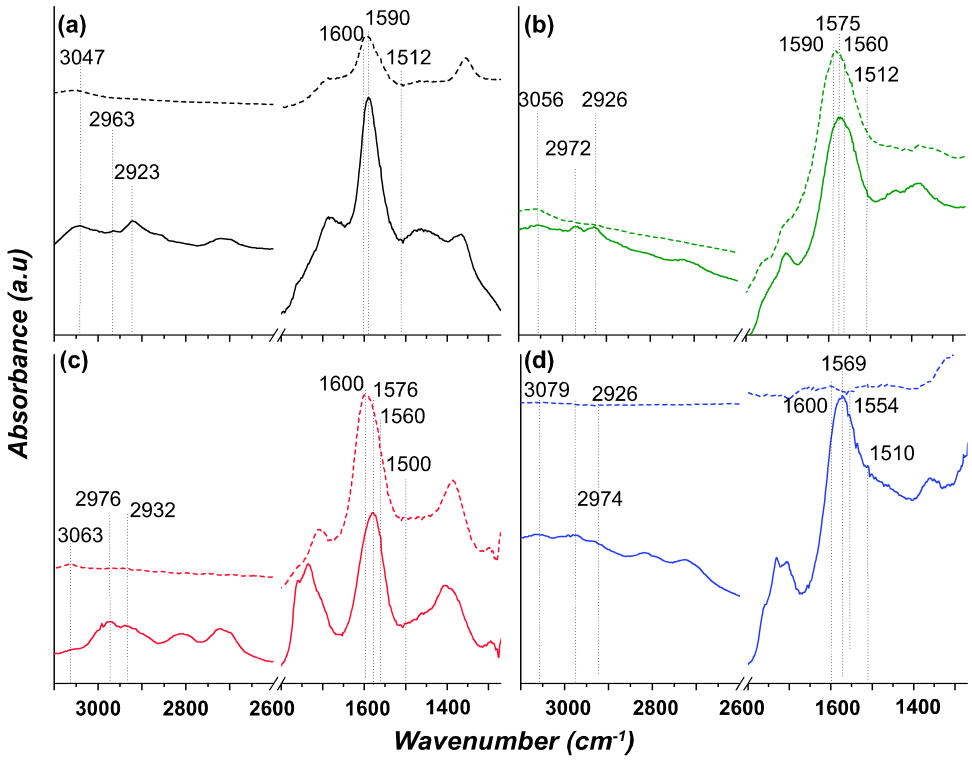

Fig. 6 Zoom-in of the FT-IR spectra of: **a** Cs-X, **b** Ca-HA, **c** Na-USY and **d** Rb-USY after 20 min of reaction (*continuous line*) and 20 min after switching off propanal and flushing with N_2 (*dashed line*)

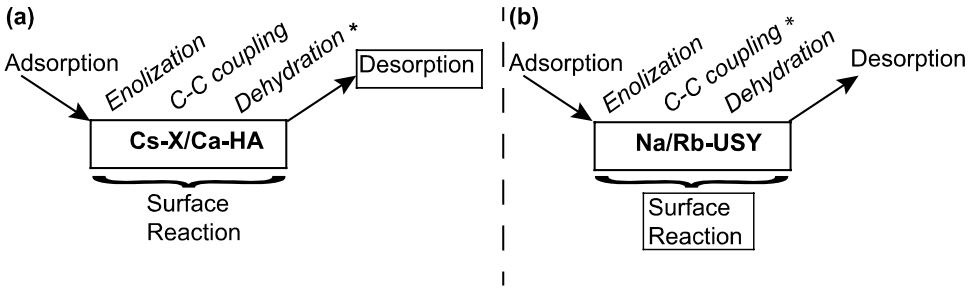

Fig. 7 Scheme of the catalytic steps for the aldol condensation reaction over: **a** Cs-X and Ca-HA, for which desorption is limiting and dehydration suggested as slowest surface reaction; **b** Na-USY and Rb-USY, where the surface reaction is limiting, with C–C coupling being the slowest step

the reaction. Furthermore, the *operando* FT-IR spectra and on-line MS data show the aldol coupling product to be present in significant amounts, suggesting that of the surface reaction steps, dehydration is the slowest (Fig. 7). In contrast, for the alkaline metal-grafted USY zeolites the surface reaction was found to be limiting, with the C–C coupling considered to be rate-determining, as intense spectral features of adsorbed propanal indicate.

Furthermore, the *operando* FT-IR/UV–Vis DRS and TGA-MS analyses provided insight into the development of carbonaceous deposits. The resistance towards coking increases in the order: Cs-X < Ca-HA < Na-USY < Rb-USY. The alkaline metal-grafted USY zeolites were more efficient in suppressing the coke formation, probably because of the moderate strength of their active sites and combination of micro- and mesoporosity. The nature of the coke was also found to differ, being strongly deficient in hydrogen (so-called hard coke) in the case of the Ca-HA catalyst. Despite noticeable coke formation on Ca-HA, the *operando* spectroscopy results do not suggest significant deactivation over the investigated time on stream.

The results thus clearly link the catalytic and physicochemical properties of each of the catalyst materials. Absence of acidity and mild basicity are most desirable for this gas phase propanal condensation. In light of overall performance, Ca-HA and the alkaline metal-grafted USY zeolites have potential, by extrapolation, for catalytic bio-oil upgrading.

Acknowledgements This work was funded by the European Union Seventh Framework Programme (FP7/2007–2013) under Grant Agreement No. 604307. M. Versluijs-Helder (Utrecht University, UU) is acknowledged for performing the TGA-MS measurements. Dr. M. U. Delgado-Jaime (UU) is highly acknowledged for helping with data fitting.

References

1. Bridgwater AV (2012) Review of fast pyrolysis of biomass and product upgrading. Biomass Bioenerg 38:68–94
2. Bertero M, de la Puente G, Sedran U (2012) Fuels from bio-oils: bio-oil production from different residual sources, characterization and thermal conditioning. Fuel 95:263–271
3. Oasmaa A, Källi A, Lindfors C, Elliott DC, Springer D, Peacocke C, Chiaramonti D (2012) Guidelines for transportation, handling, and use of fast pyrolysis bio-oil. 1. flammability and toxicity. Energy Fuels 26:3864–3873
4. Liu C, Wang H, Karim AM, Sun J, Wang Y (2014) Catalytic fast pyrolysis of lignocellulosic biomass. Chem Soc Rev 43:7594–7623
5. Vispute TP, Zhang H, Sanna A, Xiao R, Huber GW (2010) Renewable chemical commodity feedstocks from integrated catalytic processing of pyrolysis oils. Science 330:1222–1227
6. Shen W, Tompsett GA, Hammond KD, Xing R, Dogan F, Grey CP, Conner WC, Auerbach SM, Huber GW (2011) Liquid phase aldol condensation reactions with MgO-ZrO_2 and shape-selective nitrogen-substituted NaY. Appl Catal A 392:57–68
7. Shen W, Tompsett GA, Xing R, Conner C Jr, Huber GW (2012) Vapor phase butanal self-condensation over unsupported and supported alkaline earth metal oxides. J Catal 286:248–259
8. Chang Y, Ko A (2000) Vapor phase reactions of acetaldehyde over type X zeolites. Appl Catal A 190:149–155
9. Kaftan A, Schönweiz A, Nikiforidis I, Hieringer W, Dyballa KM, Franke R, Görling A, Libuda J, Wasserscheid P, Laurin M, Haumann M (2015) Supported homogeneous catalyst makes its own liquid phase. J Catal 321:32–38
10. Di Cosimo JI, Apesteguía CR (1998) Study of the catalyst deactivation in the base-catalyzed oligomerization of acetone. J Mol Catal A 130:177–185
11. Clayden J, Greeves N, Warren S (2012) Organic chemistry. 2nd edn, Oxford University Press, Oxford
12. Climent MJ, Corma A, Fornés V, Guil-López R, Iborra S (2002) Aldol condensations on solid catalysts: a cooperative effect between weak acid and base sites. Adv Synth Catal 344:1090–1096
13. Hattori H (1995) Heterogeneous basic catalysis. Chem Rev 95:537–558
14. Gangadharan A, Shen M, Sooknoi T, Resasco DE, Mallinson RG (2010) Condensation reactions of propanal over $Ce_xZr_{1-x}O_2$ mixed oxide catalysts. Appl Catal A 385:80–91
15. Verboekend D, Keller TC, Mitchell S, Pérez-Ramírez J (2013) Hierarchical FAU- and LTA-Type zeolites by post-synthetic design: a new generation of highly efficient base catalysts. Adv Funct Mater 23:1923–1934
16. Keller TC, Isabettini S, Verboekend D, Rodrigues EG, Pérez-Ramírez J (2014) Hierarchical high-silica zeolites as superior base catalysts. Chem Sci 5:677–684

17. Keller TC, Desai K, Mitchell S, Pérez-Ramírez J (2015) Design of base zeolite catalysts by alkali-metal grafting in alcoholic media. ACS Catal 5:5388–5396
18. Young ZD, Hanspal S, Davis RJ (2016) Aldol condensation of acetaldehyde over titania, hydroxyapatite, and magnesia. ACS Catal 6:3193–3202
19. Rodrigues EG, Keller TC, Mitchell S, Pérez-Ramírez J (2014) Hydroxyapatite, an exceptional catalyst for the gas-phase deoxygenation of bio-oil by aldol condensation. Green Chem 16:4870–4874
20. Tsuchida T, Yoshioka T, Sakuma S, Takeguchi T, Ueda W (2008) Synthesis of biogasoline from ethanol over hydroxyapatite catalyst. Ind Eng Chem Res 47:1443–1452
21. Hanspal S, Young ZD, Shou H, Davis RJ (2015) Multi-product steady-state isotopic transient kinetic analysis of the ethanol coupling reaction over hydroxyapatite and magnesia. ACS Catal 5:1737–1746
22. Angelici C, Weckhuysen BM, Bruijnincx PCA (2013) Chemocatalytic conversion of ethanol into butadiene and other bulk chemicals. ChemSusChem 6:1595–1614
23. Drouilly C, Krafft JM, Averseng F, Lauron-Pernot H, Bazer-Bachi D, Chizallet C, Lecocq V, Costentin G (2013) Origins of the deactivation process in the conversion of methylbutynol on zinc oxide monitored by *operando* DRIFTS. Catal Today 205:67–75
24. Delgado-Jaime MU, Mewis CP, Kennepohl P (2009) BlueprintXAS: a Matlab-based toolbox for the fitting and analysis of XAS spectra. J Synchrotron Rad 17:132–137
25. Jentoft FC (2009) Ultraviolet-visible-near infrared spectroscopy in catalysis: theory, experiment, analysis, and application under reaction conditions. Adv Catal 52:129–211
26. Lavalley JC, Lamotte J, Travert A, Czyzniewska J, Ziolek M (1998) Use of but-1-yne as a probe for the characterization of the basicity of alkali-exchanged zeolites. J Chem Soc Faraday Trans 94:331–335
27. Phung TK, Carnasciali MM, Finocchio E, Busca G (2014) Catalytic conversion of ethyl acetate over faujasite zeolites. Appl Catal A 470:72–80
28. Guzman A, Zuazo I, Feller A, Olindo R, Sievers C, Lercher JA (2005) On the formation of the acid sites in lanthanum exchanged X zeolites used for isobutane/cis-2-butene alkylation. Microporous Mesoporous Mater 83:309–318
29. Hadjiivanov KI, Vayssilov GN (2002) Characterization of oxide surfaces and zeolites by carbon monoxide as an IR probe molecule. Adv Catal 47:307–511
30. Knözinger H, Huber S (1998) IR spectroscopy of small and weakly interacting molecular probes for acidic and basic zeolites. J Chem Soc Faraday Trans 94:2047–2059
31. Diallo-Garcia S, Osman MB, Krafft JM, Casale S, Thomas C, Kubo J, Costentin G (2014) Identification of surface basic sites and acid-base pairs of hydroxyapatite. J Phys Chem C 118:12744–12757
32. Cheng ZH, Yasukawa A, Kandori K, Ishikawa T (1998) FTIR study of adsorption of CO_2 on nonstoichiometric calcium hydroxyapatite. J Chem Soc Faraday Trans 94:1501–1505
33. Hill IM, Hanspal S, Young ZD, Davis RJ (2015) DRIFTS of probe molecules adsorbed on magnesia, zirconia, and hydroxyapatite catalysts. J Phys Chem C 119:9186–9197
34. Chakarova K, Andonova S, Dimitrov L, Lagunov O, Hadjiivanov K (2016) FTIR study of CO and N_2 adsorption on [Ge]FAU zeolites in their Na- and H-forms. Microporous Mesoporous Mater 220:188–197
35. Rudakova AV, Lobo RF, Bulanin KM (2003) FT-IR Study of Carbon Monoxide Adsorption on Li-Exchanged Zeolite X. J Phys Chem B 107:5212–5220
36. Caillot M, Chaumonnot A, Digne M, van Bokhoven JA (2014) The variety of Brønsted acid sites in amorphous aluminosilicates and zeolites. J Catal 316:47–56
37. Bordiga S, Lamberti C, Bonino F, Travert A, Thibault-Starzyk F (2015) Probing zeolites by vibrational spectroscopies. Chem Soc Rev 44:7262–7341
38. Hadjiivanov K, Massiani P, Knözinger H (1999) Low-temperature CO and $^{15}N_2$ adsorption and co-adsorption on alkali cation exchanged EMT zeolites: an FTIR study. Phys Chem Chem Phys 1:3831–3838
39. Emeis CA (1993) Determination of integrated molar extinction coefficients for infrared absorption bands of pyridine adsorbed on solid acid catalysts. J Catal 141:347–354
40. Montanari T, Finocchio E, Busca G (2011) Infrared spectroscopy of heterogeneous catalysts: acidity and accessibility of acid sites of faujasite-type solid acids. J Phys Chem C 115:937–943
41. Kline CH, Turkevich J (1944) The vibrational spectrum of pyridine and the thermodynamic properties of pyridine vapors. J Chem Phys 12:300–309
42. Phung TK, Proietti-Hernández L, Lagazzo A, Busca G (2015) Dehydration of ethanol over zeolites, silica alumina and alumina: Lewis acidity, Brønsted acidity and confinement effects. Appl Catal A 493:77–8942
43. Socrates G (2001) Infrared and Raman Characteristic Group Frequencies. 3rd edn, Wiley, Chichester
44. NIST Chemistry WebBook (2005) http://webbook.nist.gov/chemistry/name-ser.html. Accessed 4 Aug 2016
45. Guirgis GA, Drew BR, Gounev TK, Durig JR (1998) Conformational stability and vibrational assignment of propanal. Spectrochim Acta Part A 54:123–143
46. Kalsi PS (2004) Spectroscopy of organic compounds. 6th edn, New Age International Publishers, New Delhi
47. Yoshino N, Akutsu H (1978) Behavior of aliphatic aldehydes to Metal(IV) Alkoxides. Bull Chem Soc Jpn 5:742–747
48. Karge HG (2001) Coke formation on zeolites. Stud Surf Sci Catal 137:707–746
49. Zhang H, Shao S, Xiao R, Shen D, Zeng J (2014) Characterization of coke deposition in the catalytic fast pyrolysis of biomass derivates. Energy Fuels 28:52–57
50. Guisnet M, Magnoux P (2001) Organic chemistry of coke formation. Appl Catal A 212:83–96
51. Qian Q, Ruiz-Martínez J, Mokhtar M, Asiri AM, Al-Thabaiti SA, Basahel SN, Weckhuysen BM (2014) Single-particle spectroscopy of alcohol-to-olefins over SAPO-34 at different reaction stages: crystal accessibility and hydrocarbons reactivity. ChemCatChem 6:772–783
52. Parvulescu AN, Mores D, Stavitski E, Teodorescu CM, Bruijnincx PCA, Gebbink RJMK, Weckhuysen BM (2010) Chemical imaging of catalyst deactivation during the conversion of renewables at the single particle level: etherification of biomass-based polyols with alkenes over H-beta zeolites. J Am Chem Soc 132:10429–10439
53. Marie O, Thibault-Starzyk F, Lavalley JC (2000) Confirmation of the strongest nitriles–hydroxy groups interaction in the side pockets of mordenite zeolites. Phys Chem Chem Phys 2:5341–5349
54. Callahan JL, Grasselli RK (1963) A selectivity factor in vapor-phase hydrocarbon oxidation catalysis. AIChE J 9:755–760
55. Puértolas B, Keller TC, Mitchell S, Pérez-Ramírez J (2016) Deoxygenation of bio-oil over solid base catalysts: from model to realistic feeds. Appl Catal B 184:77–86
56. Casale MT, Richman AR, Elrod MJ, Garland RM, Beaver MR, Tolbert MA (2007) Kinetics of acid-catalyzed aldol condensation reactions of aliphatic aldehydes. Atmos Environ 41:6212–6224
57. Pradhan AR, Wu JF, Jong SF, Tsai TC, Liu SB (1997) An ex situ methodology for characterization of coke by TGA and ^{13}C CP-MAS NMR spectroscopy. Appl Catal A 165:489–497
58. Karge HG, Nießen W, Bludau H (1996) In-situ FTIR measurements of diffusion in coking zeolite catalysts. Appl Catal A 146:339–349